Numerical simulations on the performance of optical-acoustic sensors of minimal dimensions

A Kosík[1]*, G Stojanovic[2]

1. Institut für Computational Engineering, OST Ostschweizer Fachhochschule, Werdenbergstrasse 4, 9471 Buchs, Switzerland
2. ams-OSRAM AG, Eichwiesstrasse 18b, 8645 Jona, Switzerland

ABSTRACT

This paper presents analytical and numerical methods for developing optical-acoustic transducers of minimal dimensions. One can find acoustic sensors used as microphones in various electronic devices such as smartphones or smartwatches. Therefore, it is highly desirable to minimize their size while ensuring high-quality sound reception.

The optical-acoustic sensor relies on laser detection of membrane vibrations and consists of a membrane that vibrates in the presence of an acoustic field and reflects the radiation emitted by the laser back to the laser. We focus on methods to optimize the membrane's design and the cavity (back volume) that separates the laser from the membrane. The back volume compliance significantly affects the sensitivity of the membrane. In addition, it is a noise source due to acoustic and viscous damping. Using calculations and simulations, we show the possibilities of reducing the membrane size and the air-filled back volume size while achieving the desired acoustic properties. We employ analytical calculations for the mechanical vibration of the diaphragm, back-volume compliance and resistance, and precise FEM simulations of the interaction between membrane vibration and the acoustic field. We build on similar techniques used for micromachined capacitive microphones, but we apply these methods newly to a specific setup of backplate-less optical-acoustic sensors. Based on the theoretical results, we can conclude that optical-acoustic devices achieve the same maximum noise level with smaller dimensions than the current industry standard.

1. INTRODUCTION

In recent years, the field of smart device technology has seen significant growth in the development of devices such as headsets, smartwatches, and smart speakers, all of which require high-quality audio reception capabilities. Given the small dimensions of these devices, there is an ongoing effort to create audio receivers of minimal size while maintaining a high level of sound quality. Our project aims to achieve this goal through the new design and implementation of an integrated optical microphone. This article will focus on the critical components of the optical microphone, specifically the diaphragm and the cavity defined

*Corresponding Author: adam.kosik@ost.ch

between the diaphragm and the substrate. The principle of operation for optical-acoustic sensors is based on sound sensation via the optical detection of diaphragm deflection. Acoustic pressure from sound waves causes vibrations in the diaphragm, and the deflection is detected by a laser beam that is reflected back into the laser and converted into a sensor output signal, see Figure 1. Therefore, the design of the diaphragm and cavity is crucial to the performance of this device. We consider a diaphragm with a circular shape. Besides its overall dimensions, residual stress influences its mechanical properties. The residual stress results from the fabrication. Therefore, we employ corrugations, which can reduce this stress to the desired value. For further details on the corrugated diaphragm, see patent [1], and on the optical-acoustic sensor, patents [2] and [3]. The laser used for optical detection is a vertical cavity surface emitting laser (VCSEL). We focus on a detailed description of the analytical and computational methods used to design the geometry of the optical-acoustic sensor.

In the next section, we introduce methods to optimize the design of the corrugated membrane itself. We follow the general theory for plates and shells by [4]. The mechanical behavior of micromachined flat and corrugated membranes for sensors is discussed further in articles [5-15]. We demonstrate that it is possible to substantially reduce intrinsic stress to levels that are difficult to attain for flat diaphragms. The following section deals with the air-filled cavity (back volume) that separates the laser from the diaphragm. We describe its mechanical and thermoacoustic properties. Finally, we present the coupled problem of diaphragm vibrations and thermoacoustics. Thermoacoustic effects on the movement of the diaphragm are the subject of papers [16-22].

The entire system is characterized as a coupled problem involving the interaction of compressible fluid flow and pressure-induced vibrations. In the context of fluid-structure interaction (FSI), the finite element method is often the preferred method for solving the system with a staggered or monolithic approach [23-25]. Using the Comsol software package [26], we can solve this problem as an interaction of unsteady compressible flow and structural deformation, or as a coupling of linearized compressible Navier-Stokes equations and diaphragm vibrations in the frequency domain.

Optical-acoustic transducers have been shown to possess advantages over traditional micromachined sensors. Conventional capacitive sensors detect variations in the capacitance of a capacitor composed of a front plate (diaphragm) and a backplate. A small gap between the diaphragm and the backplate is necessary to enhance sensitivity. As described by [19], thermal boundary limitations can affect the performance of micromachined microphones. In contrast, the optical-acoustic sensor does not require a backplate.

Additionally, corrugations can be incorporated to modulate the residual stress, leading to improved sensitivity and reduced acoustic noise. With optical microphones, there is no limitation with the back plate. Therefore, we can use any dimension and number of corrugations. The results of our analysis indicate the potential and limitations of optical-acoustic sensor size.

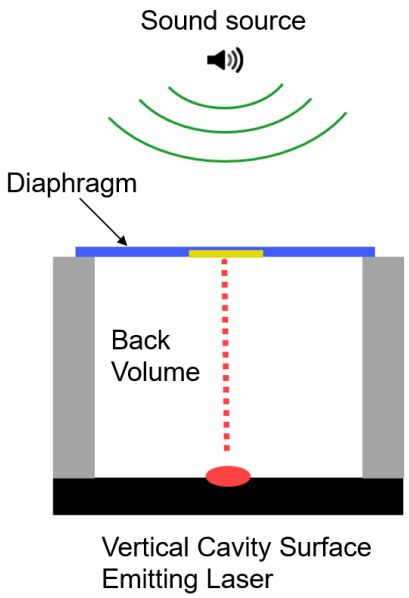

Figure 1: A sketch of the principle of an optical-acoustic sensor composed of three major components: diaphragm, laser, and cavity in the substrate between them.

2. CORRUGATED DIAPHRAGM

The initial step in the design process of the optical microphone is the design of the diaphragm. Sufficient sensitivity is required to detect membrane deflection oscillations. However, it is important to ensure that the deflection does not significantly exceed the thickness of the material, even under high loads, as nonlinear effects will occur at large displacements. In this section, we first present analytical formulae for determining both sensitivity and the rate of nonlinearity. We then describe a more accurate finite element analysis and present some results.

A comprehensive diaphragm analysis also includes determining the eigenfrequency and conducting a stress analysis. The eigenfrequency should not affect the acoustic spectrum, meaning it should be higher than 20 kHz. For designed diaphragms, the eigenfrequency is typically significantly higher. However, it is important to remember to determine the eigenfrequency for the complete system, as it may drop due to the compliance of the back volume in combination with the cavity. Stress distribution analysis results in stress concentration in the corrugations or at the edge of the diaphragm. We performed simulations for extreme pressure levels higher than that of the acoustic signal, but for this paper, we mention these properties for completeness only and do not discuss them in further detail.

2.1. Analytical Calculation of Characteristics

We consider the diaphragm of the sensor as a circular plate with clamped edges. We start with the description of small deformations. Then, we extend the formulation to include the effect of residual tensile stress and its reduction by corrugations. Finally, we add the nonlinear behavior at large deflections.

The approximate formula for flat circular plates is described in [4, pp. 55]. We consider a rigidly clamped plate carrying a uniform load of intensity p the deflection w of the membrane has been described by $w(r) = \frac{p}{64D}(a^2 - r^2)^2$.

The deflection could also be expressed as in [15] with the aid of the maximum deflection w_0 as

$$w(r) = w_0 \left(1 - \frac{r^2}{a^2}\right)^2, \tag{1}$$

where the maximum deflection is at the center of the plate

$$w_0 = \frac{pa^4}{64D}. \tag{2}$$

Here,

- a radius, $a > 0$,
- r radial coordinate, $r \in [0, \mathrm{a}]$,
- w deflection, w: $[0, \mathrm{a}] \to \mathrm{R}$,
- h thickness, $h > 0$,
- p intensity of the distributed load, $p \in R$,
- D bending rigidity,

$$D = \frac{Eh^3}{12(1-\nu^2)}, \tag{3}$$

- E modulus of elasticity, $E > 0$,
- ν Poisson's ratio, $\nu \in (0, 0.5)$.

The slope φ of the deflection w is

$$\varphi(r) = -\frac{\partial w}{\partial r} = \frac{pr}{16D}(a^2 - r^2), \tag{4}$$

the radial stress $\sigma_r$reads

$$\sigma_r(r) = \frac{3p}{8h^2}\left(a^2(1+\nu) - r^2(3+\nu)\right), \tag{5}$$

and tangential stress σ_t

$$\sigma_t(r) = \frac{3p}{8h^2}\left(a^2(1+\nu) - r^2(1+3\nu)\right). \tag{6}$$

The stresses are equal in the center of the membrane

$$\sigma_r(0) = \sigma_t(0) = \frac{3pa^2}{8h^2}(1+\nu) \tag{7}$$

The value of the radial stress is faster decreasing. At the boundary of the plate

$$\sigma_r(a) = -\frac{3pa^2}{4h^2}, \tag{8}$$

and

$$\sigma_t(a) = -\frac{3pa^2\nu}{4h^2}. \tag{9}$$

Consider a flat membrane as a circular plate as in [4, pp. 391] submitted to the simultaneous action of a symmetrical lateral load and a uniform tension in the middle of the plate. As shown in [4, pp. 392-393], we can express the maximum deflection in the middle of the membrane ($r = 0$) as

$$w = \frac{p}{K_{tot}}, \tag{10}$$

where $K_{tot} = K_1(1 - \alpha)$, $\alpha = \frac{\sigma a^2}{14.68D}$. Then the bending stiffness is

$$K_1 = \frac{64\pi}{a^2} D, \tag{11}$$

and the stiffness component $K_2 = K_1\alpha$ due to the residual stress is

$$K_2 = \frac{64\pi}{a^2} D\alpha = \frac{64\pi}{a^2} D \frac{\sigma a^2}{14.68D} = \frac{64\pi\sigma}{14.68} = 4.36\pi\sigma. \tag{12}$$

Considering large deflections, the approximate formulae for uniformly loaded circular plates must be modified. The deflection is considered large if the membrane's middle plane's strain can not be neglected. In practice, we denote as large the deflections three times bigger than the thickness of the plate. The effect of stretching can be approximated according to [15] by the term $\frac{16}{35}\frac{w_0^2}{h^2}$. Similar approximation $0.488\frac{w_0^2}{h^2}$ is in [4, pp. 400-402]. Because of this effect, the relation between the deflection w_0 and the pressure p becomes nonlinear.

Let us express the approximate formula for large deflection of the plate

$$w(r) = w_0\left(1 - \frac{r^2}{a^2}\right)^2, \tag{13}$$

where it holds

$$w_0 = \frac{p}{\frac{4.36h}{a^2}\sigma_0 + \frac{64}{a^4}D\left(1 + \frac{16w_0^2}{35h^2}\right)}. \tag{14}$$

Equivalently, we can express the pressure as a function of the deflection

$$p = \left(\frac{4.36h}{a^2}\sigma_0 + \frac{64}{a^4}D\right)w_0 + \frac{16}{35}\frac{64}{a^4}D\frac{w_0^3}{h^2}. \quad (15)$$

The stiffness of the plate increases with the deflection. We may define the linear and nonlinear stiffness

$$\mathrm{K_{lin}} = \frac{4.36\mathrm{h}}{\mathrm{a}^2}\sigma_0 + \frac{64}{\mathrm{a}^4}\mathrm{D}, \qquad \mathrm{K_{non}} = \frac{16}{35}\frac{64}{\mathrm{a}^4\mathrm{h}^2}\mathrm{D} \quad (16)$$

The difference in percentage between the deflection calculated with the stretching of the middle surface taken into account and the deflection obtained by neglecting this stretching is known as the total harmonic distortion (THD). We are interested in cases where the stretching is significant, meaning when the distortion is greater than 1%, 3%, or 10%. When the distortion reaches 10%, the microphone is considered to have reached an overload point at which it can no longer function effectively as a sound sensor. The calculation of the deflection for a given THD is straightforward:

$$w_0 = \frac{\mathrm{THD}}{1-\mathrm{THD}}\frac{K_{lin}}{K_{non}}. \quad (17)$$

In most cases, the diaphragm is characterized by sensitivity, the slope of the linear relationship between deflection w_0 and pressure intensity p. The sensitivity is compared with the sound level at which the distortion reaches 10%. The goal of the design is to achieve a high sensitivity while keeping the overload point above 135 dB. The material of the diaphragm is usually given, so the task is to find the optimal relationship between the diameter, thickness, and tension stress of the diaphragm. A crucial aspect of this is the design of the corrugations.

2.2. Corrugations

In order to reduce internal stress, the use of corrugations is employed. This section will summarize the analytical methods used to determine stress reduction. Various techniques exist for obtaining approximate equations for circular plates with corrugations. In [5] and [6] is examined the use of a formula for a corrugated membrane that is initially assumed to be stress-free. The authors discuss the large deformation and stress reduction in the membrane. A similar assumption of a stress-free membrane is also presented in [4]. Another formula for stress reduction resulting from corrugations can be found in [9]. The approach taken by [10] and [11] is similar to the studies mentioned above. They introduce an additional calculation for stress reduction, and they summarize this in a formula that includes the bending stiffness, residual stress stiffness, and nonlinear stretching. Additionally, the deflection of a corrugated membrane is also discussed in [13], including a formula for the modifying factor of stiffness increase by a center boss. According to [6], following [5]

$$p = a_p\frac{Eh^3}{a^4}w_0 + b_p\frac{Eh}{(1-\nu^2)a^4}w_0^3, \quad (18)$$

where

$$a_p = \frac{2(q+1)(q+3)}{3\left(1-\frac{\nu^2}{q^2}\right)}, \qquad b_p = 32\frac{1-\nu^2}{q^2-9}\left(\frac{1}{6}-\frac{3-\nu}{(q-\nu)(q+3)}\right) \tag{19}$$

and for a sinusoidal corrugation profile

$$q^2 = \frac{s}{l}\left(1+\frac{3}{2}\frac{H^2}{h^2}\right), \tag{20}$$

where q is a corrugation profile factor, H is the height of corrugations, s is the corrugation arc length, and l is the corrugation's spatial period.

For shallow corrugations ($H << l$), the shape of corrugations has only a minor influence on the profile factor q. For a rectangular corrugation profiles.

$$\frac{s}{l} = \frac{a+2NH}{a}, \tag{21}$$

where N is the number of corrugations. Stress is reduced as

$$\sigma = \frac{\sigma_0 b_p}{2.83}. \tag{22}$$

According to [9], stress is reduced as

$$\sigma = \frac{\sigma_0}{1+\sin(\beta)\frac{H^2}{h^2}\frac{Nw}{a-N(w+b)}}. \tag{23}$$

According to [4, pp. 404], if the corrugation follows a sinusoidal law and the number of waves along a diameter is sufficiently large ($N > 5$), the following expression may be used:

$$p = \left(8\frac{Eh^3}{a^4}\frac{H^2}{h^2}+\frac{64}{a^4}D\right)w_0 + \frac{9}{56}\frac{64}{a^4}D\frac{w_0^3}{h^2}. \tag{24}$$

According to [10] and [11], the formula for the pressure deflection relationship is

$$p = \left(a_p\frac{Eh^3}{a^4}+4\frac{h\sigma}{a^2}\right)w_0 + b_p\frac{Eh}{(1-\nu)^2a^4}w_0^3, \tag{25}$$

where a_p and b_p are the same as above in the paragraph. The equilibrium stress σ in a corrugated diaphragm is given by

$$\sigma = \frac{ah^2}{ah^2+6NH^2w\sin(\beta)+8NH^3w\sin^2(\beta)}\sigma_0. \tag{26}$$

The analytical relations discussed in this and the previous section are valuable for the initial design of diaphragms. We have developed a straightforward algorithm to calculate the sensitivity and the distortion for a given geometrical and material parameters. However, finite element simulations are recommended for more accurate results, especially for corrugated diaphragms.

2.3. Finite-Element Analysis

We used Comsol software [23] based on the finite element method to analyze the mechanical behavior of the diaphragm. We applied the solid mechanics' module to solve the standard elasticity equations, considering the material's tensile prestress and geometric nonlinearity. We analyzed both the static behavior and the eigenfrequencies of the diaphragm. Moreover, we were able to use an axisymmetric model due to the rotational symmetry of the model.

We have defined axial symmetry at the center of the model. A uniformly distributed pressure force of intensity p is applied in the normal direction on the upper surface. At the perimeter diaphragm is fixed to the substrate, resulting in zero displacements. The lower boundary is not subject to any constraints or loads. Figure 2 is an example of a deformed diaphragm with a diameter of 300 µm attached to the substrate for the static load of 112 Pa, which is approximately 135 dB SPL.

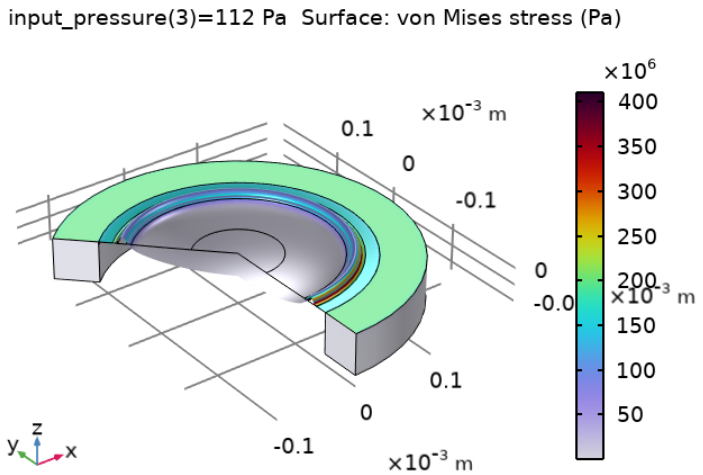

Figure 2: Visualization of the static deformation (scaled 20x) of a corrugated diaphragm with a diameter of 300 µm attached to the substrate for the static load of 112 Pa.

2.4. Results

We conducted a computational study of the mechanical behavior of silicon nitride diaphragms of diameters 1 mm, 500 µm, and 300 µm, respectively. The objective of the study was to achieve a sensitivity of 20 nm/Pa and linear progression under a load in the dynamic range. The nonlinear effects of stretching were also taken into consideration. The linear deflection of the diaphragms was extrapolated and compared to the deflection calculated through simulation. The aim was to maintain a distortion of less than 10% between the extrapolated and simulated deflection values in the dynamic range, i.e., up to 135 dB.

The material characteristics of silicon nitride are summarized in Table 1. The silicon substrate was assumed to be a rigid body in the simulations, and the small aluminum mirror placed in the center of the diaphragm was neglected as its effect on the mechanical behavior of the diaphragm was not relevant to the methodology presented in this paper.

Table 1: Material Characteristics

Material	**Silicon Nitride**
E - Young elasticity modulus	166 [GPa]
ν - Poisson's ratio	0.23
ϱ – Density	3170 [kg.m^{-3}]

First, we compared the distortion of flat and corrugated diaphragms of different sizes but with similar sensitivity. To achieve similar sensitivity, the residual stress of the flat diaphragms and the dimensions of the corrugated diaphragms were systematically varied. The thicknesses of the smaller membranes were also reduced to achieve the desired sensitivity of about 20 nm/Pa. A summarized comparison can be found in Table 2. Corrugated diaphragms provide the desired sensitivity with better linearity at high deflection. While smaller diaphragms were not the target size for the intended application, they show the potential but also the limits of further minimizing the size of the diaphragms. The diaphragm of 500 µm diameter can almost reach the limit of 10% THD for 135 dB.

Table 2: Comparison of THD for flat and corrugated diaphragms of different diameters d and thickness h with similar sensitivity.

d [µm]	**h [nm]**	**Res. stress [MPa]**	**Corrugations # / [µm]**	**Sensitivity [nm/Pa]**	**THD 135 dB [%]**
1000	250	12	flat	20.04	13.53
500	50	15	flat	20.57	27.72
300	50	5.1	flat	20.80	54.83
1000	250	200	5 / 10x1.1	20.13	4.22
500	50	200	1 / 10x0.65	20.50	12.23
300	50	200	1 / 10x0.65	20.37	32.72

Additionally, a sensitivity analysis of the corrugation parameters was performed for a 1 mm diameter diaphragm with a thickness of 250 nm. The default settings assumed a uniform intrinsic stress of 200 MPa, which was reduced by using five corrugations with a width of 10 micrometers and a depth of 1.1 micrometers. The corrugations were assumed to have an idealized rectangular shape and were evenly distributed. The distance of the corrugations from the perimeter was 35 micrometers.

Table 3 compares sensitivity and distortion under variations of intrinsic stress. The aim of the fabrication process should be to achieve the most uniform distribution of tensile stress to optimize the diaphragm's performance.

In Table 4, we see the results for the variations in the corrugation depth. This comparison's results show that changes in the corrugation depth significantly affect the diaphragm's sensitivity and distortion. Therefore, we can conclude that the corrugation depth is the most influential parameter on the mechanical behavior of the diaphragm.

Table 5 presents a comparison of sensitivity and distortion for corrugated diaphragms with varying corrugation widths. We may expect that any inaccuracies in the width of the corrugations during fabrication will not significantly impact the mechanical behavior of the diaphragm.

Similarly, it is not easy to achieve perfectly square corrugations in manufacturing. Table 6 compares corrugations with 90 and 45 degrees of inclination and rounded corners. The rounded corners have a radius of half the depth of the corrugations. We can conclude that the influence of the shape of the corrugations is not significant, but a slight reduction in the sensitivity of the diaphragm must be considered.

Table 3: Comparison of sensitivity and distortion under variations of residual stress for the diaphragm of diameter $d = 1\ mm$ and thickness $h = 250\ nm$.

d [µm]	h [nm]	Res. stress [MPa]	Corrugations # / [µm]	Sensitivity [nm/Pa]	THD 135 dB [%]
1000	250	150	5 / 10x1.1	28.98	10.02
1000	250	200	5 / 10x1.1	20.13	4.22
1000	250	250	5 / 10x1.1	14.97	1.91

Table 4: Comparison of sensitivity and distortion under variations of corrugations' depth for the diaphragm of diameter $d = 1\ mm$ and thickness $h = 250\ nm$.

d [µm]	h [nm]	Res. stress [MPa]	Corrugations # / [µm]	Sensitivity [nm/Pa]	THD 135 dB [%]
1000	250	200	5 / 10x1.0	15.13	1.99
1000	250	200	5 / 10x1.1	20.13	4.22
1000	250	200	5 / 10x1.2	26.37	8.17

Table 5: Comparison of sensitivity and distortion under variations of corrugations' width for the diaphragm of diameter $d = 1\ mm$ and thickness $h = 250\ nm$.

d [µm]	h [nm]	Res. stress [MPa]	Corrugations # / [µm]	Sensitivity [nm/Pa]	THD 135 dB [%]
1000	250	200	5 / 8x1.1	16.16	2.28
1000	250	200	5 / 10x1.1	20.13	4.22
1000	250	200	5 / 12x1.1	24.44	7.12

Table 6: Comparison of sensitivity and distortion under variations of corrugations' shape for the diaphragm of diameter $d = 1\ mm$ and thickness $h = 250\ nm$.

d [µm]	h [nm]	Res. stress [MPa]	Corrugations # / [µm]	Sensitivity [nm/Pa]	THD 135 dB [%]
1000	250	200	5 / 10x1.1 A	20.13	4.22
1000	250	200	5 / 10x1.1 B	17.95	3.10
1000	250	200	5 / 10x1.1 C	17.61	2.94

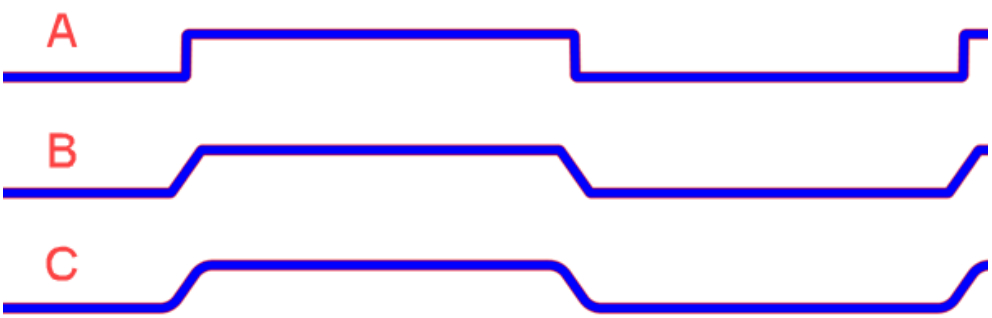

Figure 3: Three corrugation shapes with different inclination angles and corner rounding.

3. ACOUSTIC SENSOR CAVITY

When considering the dimensions of the optical-acoustic sensor, it is necessary not to neglect the influence of air in the cavity volume enclosed between the substrate and the diaphragm. There is an effect of the compliance of the back volume on the sensitivity of the diaphragm and the mechanical-thermal noise, which is expected to be the dominant noise component in the whole acoustic spectrum. Therefore, we must consider the air's compressibility and calculate the compliance of the back chamber and the mechanical-thermal noise as described in [17] and calculate the noise. Mechanical-thermal noise is caused by fluctuating forces, which are directly related to all the dissipative mechanisms. We can describe the membrane as a mechanical oscillator in which damping is given by mechanical resistance, see [17]. In general, we shall consider any dissipative mechanism that allows energy to escape, e.g., acoustic and viscous dissipations, support dissipations, and internal and material-related dissipations. Nevertheless, the acoustic and viscous dissipations caused by the surrounding air are dominant, and the noise caused by the other dissipations is very low, see [18]. We want to investigate the case when the diaphragm and cavity become smaller.

An advantage to the standard condenser sensors is that we do not need to consider the proximity of a few micrometers of the membrane to the backplate, see [20]. In our construction, the closest wall will be more than the distance of 50 μm, which is necessary for the laser beam.

Furthermore, the analysis of individual noise contributions is also analyzed in [19] or, more generally, in [21]. Based on these findings, we conclude that thermoacoustic noise will be the primary noise source for the proposed optical-acoustic sensor.

3.1 Back volume and total compliance

In order to obtain the sensitivity of the diaphragm with the back volume, we need to calculate the compliance of the diaphragm, the back volume, and finally, total compliance. The compliance of a diaphragm C_{mbr} is given by

$$C_{mbr} = \frac{\pi a^2}{3} S_0, \tag{27}$$

where a is the radius of the diaphragm and S_0 is the static sensitivity of the diaphragm, or we can also describe it as a sensitivity in a vacuum.

The closed back chamber or back volume occupied by air also behaves like a spring. The compliance of the back chamber depends on its volume and compression modulus of the air:

$$C_{bv} = \frac{V_{bv}}{K_{air}} = \frac{\pi r_{bv}^2 h_{bv}}{K_{air}}, \tag{28}$$

where V_{bv} is the volume of the back chamber, r_{bv} and h_{bv} its radius and height, respectively. K_{air} is the compression modulus of the air. In the calculations below, we set $K_{air} = 101\ kPa$, the isothermal bulk modulus.

Total compliance is equal to the reciprocal of the sum of the reciprocal compliances. For the case of two compliances, the total compliance is equal to

$$C_{tot} = \frac{C_{mbr} C_{bv}}{C_{mbr} + C_{bv}}. \tag{29}$$

In Table 7, we compare the compliance of the diaphragm and of the back volume. The compliance of the membrane corresponds to a sensitivity of 20 nm/Pa for a static deflection. We see that for all the sizes of the membranes and chosen back volume height, the compliances are in the same order. Therefore, the size of the back volume influences the total compliance and the sensitivity of the back volume. The last column shows how the effect of back volume will reduce the total sensitivity of the membrane S_{tot}. Furthermore, we show in Figure 4 how the sensitivity and compliance of the whole system change depending on the varying size of the back volume for the 1 mm diameter membrane.

Table 1: Comparison of the total compliance C_{tot}, membrane compliance C_{mbr}, back volume compliance C_{bv}, sensitivity S_{tot} for varying back volume V_{bv} of height h_{bv} and diameter d.

d [µm]	h_{bv} [µm]	V_{bv} [mm^3]	C_{mbr} [m^3/Pa]	C_{bv} [m^3/Pa]	C_{tot} [m^3/Pa]	S_{tot} (rms/peak) [nm/Pa]
1000	300	0.236	5.24E-15	2.33E-15	1.61E-15	6.16 / 8.72
1000	500	0.393	5.24E-15	3.88E-15	2.23E-15	8.52 / 12.05
1000	1000	0.785	5.24E-15	7.78E-15	3.13E-15	11.95 / 16.90
500	500	0.098	1.31E-15	9.72E-16	5.86E-16	8.52 / 12.05
300	500	0.035	4.71É-16	3.50E-16	2.01E-16	8.52 / 12.05

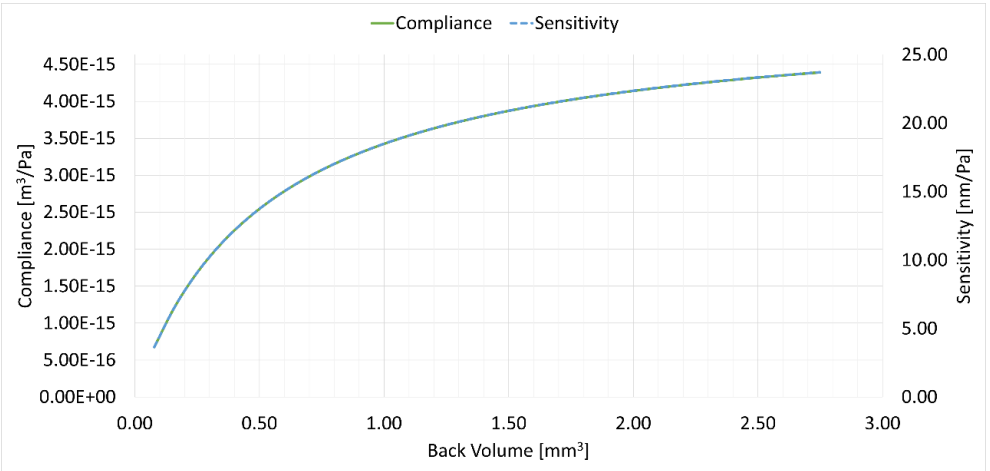

Figure 4: Compliance and sensitivity for varying sizes of the back volume.

3.2 Thermo-acoustic noise

Figure 5 demonstrates the temperature changes in the cavity on a comparison of temperature variations for frequencies of 100 Hz, 1 kHz, and 20 kHz. Assuming the isothermal boundaries, we can observe that the thermal boundary layer size depends on the frequency of the movement. The thickness of the thermal boundary layers can be approximated by the formula [19]

$$h_{TBL} = \sqrt{\frac{\kappa}{\varrho_0 C_p \pi f}}, \tag{30}$$

where ϱ_0 is the density, κ is the thermal conductivity and C_p is the specific heat at constant pressure of the air. For lower frequencies, the thermal boundary layers fill the whole cavity.

We will use the formulae presented in [16, 17] to describe the noise produced by the agitation of air molecules. The Johnson-Nyquist noise pressure spectral density is expressed as

$$p_A(f) = \sqrt{4k_B T_0 R_A(f)}, \tag{31}$$

where $k_b = 1.38 \cdot 10^{-23}[J/K]$ is Boltzmann's constant, T_0 is the absolute temperature and R_A is the acoustic resistance. In practice, the overall noise level for the entire acoustic spectrum is obtained by integrating the spectral density and evaluated in dB. Also,

the different perception of the human ear shall be taken into account. Hence, we apply the A-filtering. We calculate the A-weighted sound pressure level using the frequency-dependent weighting amplitude function w:

$$w(f) = \frac{12194^2 f^4}{(f^2+20.6^2)\sqrt{f^2+107.7^2}\sqrt{f^2+737.9^2}(f^2+12194^2)} \tag{32}$$

The A-weighted sound pressure level results from the integration formula

$$Lp_{Aw} = 20\log\left(\frac{1}{p_{ref}}\sqrt{\int_{20}^{20000} {p_A}^2(f)w^2(f)\,df}\right). \tag{33}$$

For the precise estimation of the acoustic resistance R_A we employ the Thermoviscous Acoustic module in Comsol [26]. The resistance can be computed as the resistive part of the acoustic impedance $Z_{ac} = p/Q_D$, where p is the pressure load and Q_D is the diaphragm volume velocity. The alternative way described in the Comsol manual [26] is a determination of the resistance through the dissipated and viscous heat in the cavity.

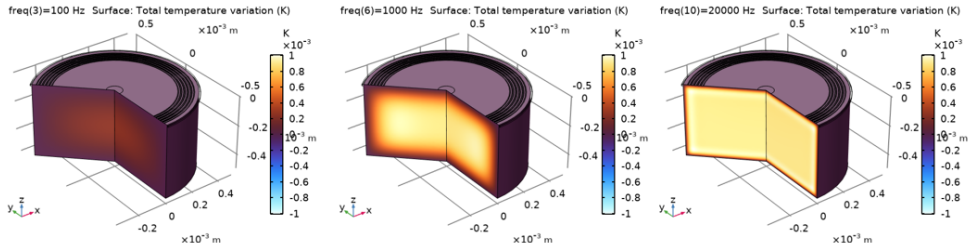

Figure 5:Total temperature variation for frequencies of 100 Hz, 1 kHz, and 20 kHz for a diaphragm of diameter 1 mm and cavity of height 500 μm.

4. ACOUSTIC-STRUCTURE INTERACTION

Let us describe the FEM simulation of the complete system of the interaction of thermoacoustic flow and diaphragm vibrations. The settings of the solid mechanics part of the problem are similar to the one described in Section 2. However, it differs in the boundary conditions on the upper and lower boundary of the diaphragm. On the upper boundary, we still prescribe uniform pressure load, but as a harmonic wave of a prescribed frequency in the acoustic frequency range from 20 Hz to 20 kHz. On the lower boundary, we define the coupling condition. The air pressure load acting on the boundary coming from the thermoacoustic flow and the velocity of the diaphragm vibrations is a boundary condition for the fluid flow.

The thermoacoustic air flow in the cavity is described with the linearized compressible Navier-Stokes equations. On the walls of the cavity is prescribed no-slip condition and a zero velocity except for the common boundary of the cavity and diaphragm, where the velocity equals the deformation velocity as described above. We consider the surrounding temperature of 293.15 K and the isothermal wall boundary condition. In [19], the authors compared the adiabatic and isothermal boundary conditions. For the noise calculation, the isothermal boundary conditions lead to higher noise. Therefore, we do not expect our model to be underestimating the noise.

As in Section 2, the computational domain is rotationally symmetric. Therefore, we can simplify the model to an axisymmetric setting. The governing system is formulated in the frequency domain. We choose a set of frequencies with a logarithmic distribution. The simulation results are interpolated with a piecewise linear function, which is used for the integration formulae.

We obtained using Comsol FE analysis noise and sensitivity approximations for different settings. In Table 8, we can compare the results for the corrugated and flat diaphragm of diameter 1 mm with a cylindrical back volume of the same diameter and height of 500 μm. The system with a corrugated diaphragm can reach higher sensitivity. However, the sensitivities are significantly lower than the static deflection without the effect of back volume. The computed noise is almost the same. Simulations with smaller diameter membranes show similarly lower sensitivity but higher noise values. This results from the fact that although we consider the same cavity height, the size of the back volume is naturally smaller due to the smaller diameter.

Increased sensitivity can be achieved, for example, by increasing the depth of the corrugations, as shown in Figure 6, or by adding more corrugations, Figure 7. The noise values do not change significantly. The sensitivity will also be affected by the residual stress value due to the manufacturing process. However, as can be seen in Figure 8, variations of an order of magnitude of a few MPa result in a change in sensitivity of less than one nm/Pa. In order to achieve a decrease in the noise, we need to increase the size of the back volume. Figure 9 shows that with a volume of about 1 mm3 we get to a noise level of about 20 dBA SPL. This noise level corresponds to a very quiet environment. These are promising results for the packaging, but on the other hand, they demonstrate the limits of the performance of the optical-acoustic sensors.

Table 2: Sensitivity S_{tot} and noise values obtained using Comsol for different diaphragm diameters d, thickness h, intrinsic stress σ_0 and back volume height h_{bv}.

d [μm]	h [nm]	h_{bv} [μm]	σ_0 [MPa]	Corrugations #: WxH [μm]	S_{tot} (rms/peak) [nm/Pa]	Noise SPL [dBA]
1000	250	500	12	Flat	5.87 / 8.30	25.41
1000	250	500	200	5: 10 x 1.1	7.23 / 10.23	25.37
500	50	500	200	1: 10 x 0.65	6.28 / 8.89	32.07
300	50	500	200	1: 10 x 0.65	7.49 / 10.59	36.77

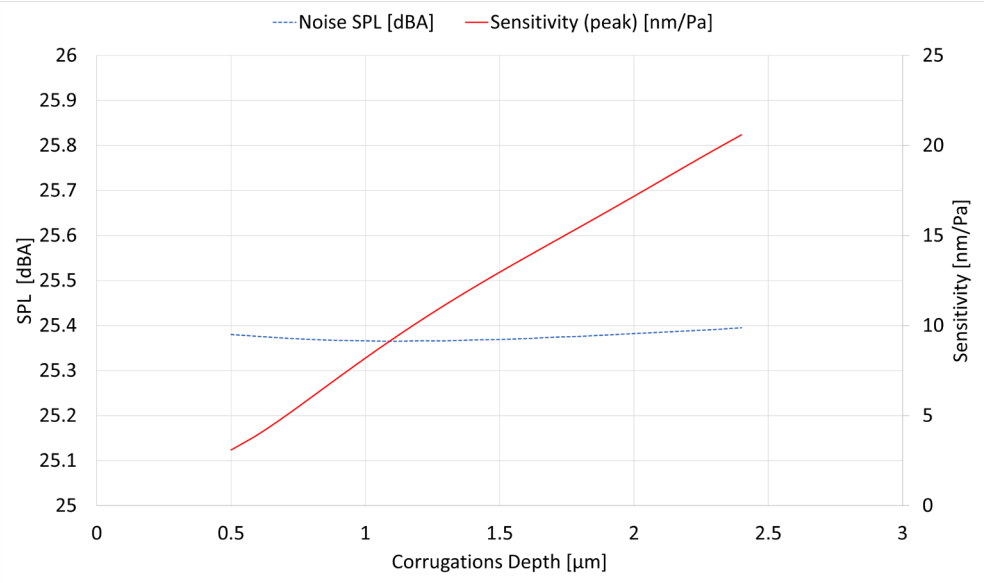

Figure 6: Noise and sensitivity obtained using Comsol for different depths of 5 corrugations of width 10 µm for a diaphragm of diameter 1 mm, thickness 250 nm, intrinsic stress 200 MPa, and back volume height of diameter 1 mm and height 500 µm.

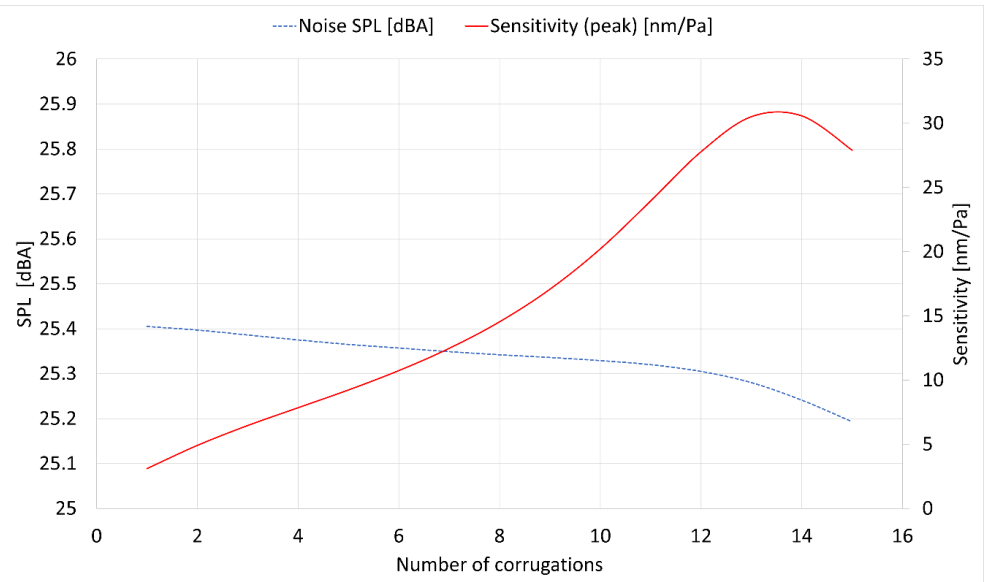

Figure 7: Noise and sensitivity obtained using Comsol for different numbers of corrugations of height 1.1 µm and width 10 µm for a diaphragm of diameter 1 mm, thickness 250 nm, intrinsic stress 200 MPa and back volume height of diameter 1 mm and height 500 µm

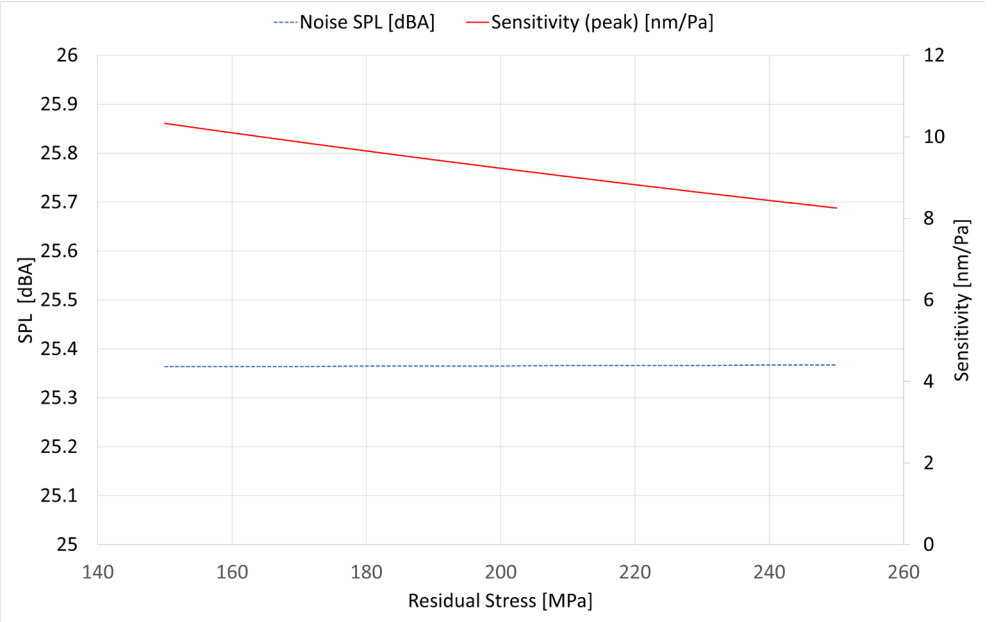

Figure 8: Noise and sensitivity obtained using Comsol for different values of residual stress for a diaphragm of diameter 1 mm, thickness 250 nm, and intrinsic stress 200 MPa with 5 corrugations of height 1.1 µm, and width 10 µm and back volume height of diameter 1 mm and height 500 µm.

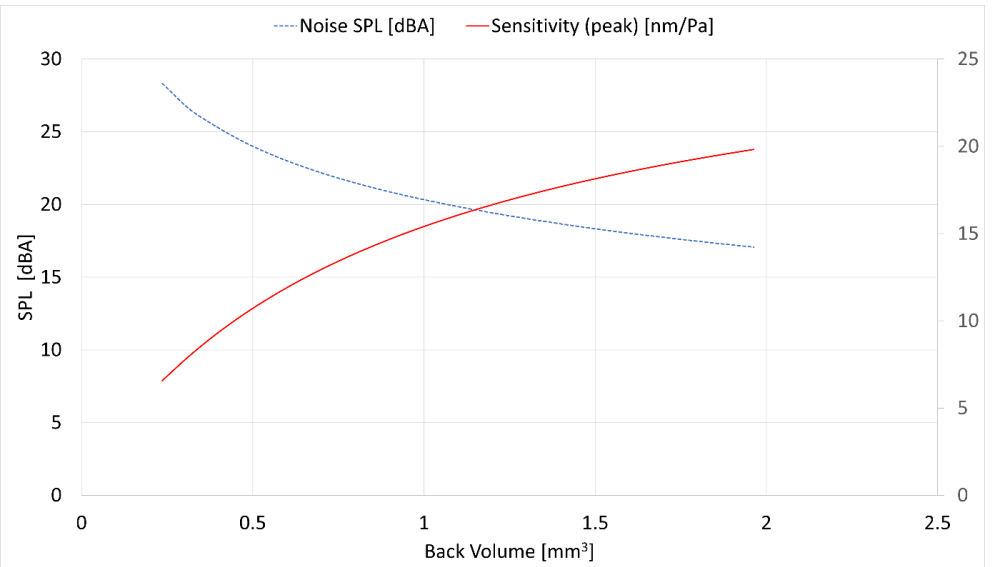

Figure 9: Noise and sensitivity obtained using Comsol for different sizes of the back volume of diameter 1 mm for a diaphragm of diameter 1 mm and thickness 250 nm with 5 corrugations of height 1.1 µm and width 10 µm.

5. CONCLUSION

We have presented an overview of analytical and simulation methods used for the design of novel optical-acoustic sensors of minimal dimension.

The main results are outcomes of the finite-element simulations. For rapid development, we can use algorithms based on formulae, which are analytical solutions of the differential equations of the base problem. However, as a main advantage of the theoretical approach, we find that one can understand the crucial principles of the system. For the diaphragm mechanical characteristics, we can understand that the trade-off between sensitivity and linearity consists primarily in reducing residual stress by the corrugations to values still high enough to avoid the nonlinear stretching for higher load. Furthermore, it allows us to understand that the back volume design is important for the sensitivity of the membrane itself. Back volume is also the primary source of thermo-viscous noise. It is supposed to be dominant in the whole acoustic spectrum.

We can summarize that the necessary minimal size of the back volume limits the reduction of the size of the optical-acoustic sensor. The compliance of the back volume is also an essential factor for the sensitivity of diaphragms, which we can influence by designing corrugations under sufficiently low total harmonic distortion. The presented results are for the axisymmetric model of these main components. In practice, we must take into account the packaging requirements. This article also focuses only on the methodology and theoretical results. In the next phase of the project, prototype sensor measurements will follow. In the future, we can also present results for other essential topics, namely protective screen design and robustness.

ACKNOWLEDGEMENTS

This work was co-financed by Innosuisse under project no. 58117.1 IP-ENG in partnership with ams-OSRAM AG. We would also like to thank our colleagues who worked on this project. Namely, Peter Heeb, who was involved in the initial stages of the design and whose work we have built on.

REFERENCES

[1] Stojanovic G, Steele C, Mueller S, Froehlich T, inventors; AMS AG, assignee. Sensors with Corrugated Diaphragms. WO 2020/083791 A1 (WIPO patent) 2020. https://patents.google.com/patent/WO2020083791A1

[2] Seurin J-F, Stojanovic G, Nevou L, inventors; AMS Sensors Asia Pte.Ltd., assignee. Sensing Methods and Sensing Systems. WO 2021/158176 A1 (WIPO patent) 2021. https://patents.google.com/patent/WO2021158176A1

[3] Stojanovic G, Seurin J-F, Xu G, Wang H, Gao P, inventors; AMS International AG, assignee. Optical Acoustic Sensor. WO 2022/084443 A1 (WIPO patent) 2022. https://patents.google.com/patent/WO2022084443A1

[4] Timoshenko S, Woinowsky-Krieger S. Theory of plates and shells. New York: McGraw-hill; 1959 Dec.

[5] Di Giovanni M. Flat and corrugated diaphragm design handbook. Marcel Decker. Inc, New York, page 130ff, 1982. 8, 9.

[6] Scheeper PR, Olthuis W, Bergveld P. The design, fabrication, and testing of corrugated silicon nitride diaphragms. Journal of microelectromechanical systems. 1994 Mar;3(1):36-42.

[7] Bitsie, F., Eaton, W.P., Plummer, D.W. and Smith, J.H., 1999. A new analytical solution for diaphragm deflection and its application to a surface-micromachined pressure sensor (No. SAND99-0573C). Sandia National Lab.(SNL-NM), Albuquerque, NM (United States); Sandia National Lab.(SNL-CA), Livermore, CA (United States).

[8] Castellanos-Gomez A, Singh V, van der Zant HS, Steele GA. Mechanics of freely-suspended ultrathin layered materials. Annalen der Physik. 2015 Jan;527(1-2):27-44.

[9] Fuldner M, Dehe A, Lerch R. Analytical analysis and finite element simulation of advanced membranes for silicon microphones. IEEE Sensors Journal. 2005 Sep 6;5(5):857-63.

[10] Taybi M, Azizollah Ganji B. Modelling of resonance frequency of MEMS corrugated diaphragm for capacitive acoustic sensors. International Journal of Engineering. 2014 Dec 1;27(12):1850-4.

[11] Azizollah Ganji B, Taybi M. The Effect of Corrugations on Mechanical Sensitivity of Diaphragm for MEMS Capacitive Microphone. International Journal of Engineering, 2013; 26(11): 1323-1330.

[12] Hong S, Weihs TP, Bravman JC, Nix WD. Measuring stiffnesses and residual stresses of silicon nitride thin films. Journal of Electronic Materials. 1990 Sep;19(9):903-9.

[13] Jerman JH. The fabrication and use of micromachined corrugated silicon diaphragms. Sensors and Actuators A: Physical. 1990 Apr 1;23(1-3):988-92.

[14] Schellin R, Hess G, Kühnel W, Thielemann C, Trost D, Wacker J, Steinmann R. Measurements of the mechanical behaviour of micromachined silicon and silicon-nitride membranes for microphones, pressure sensors and gas flow meters. Sensors and Actuators A: Physical. 1994 Apr 1;41(1-3):287-92.

[15] Schomburg WK. Introduction to microsystem design. Springer; 2015 Jun 25.

[16] Gabrielson TB. Fundamental noise limits in miniature acoustic and vibration sensors. NAVAL AIR DEVELOPMENT CENTER WARMINSTERPA MISSION AVIONICS TECHNOLOGY DEPT; 1991 Dec 31.

[17] Gabrielson TB. Mechanical-thermal noise in micromachined acoustic and vibration sensors. IEEE transactions on Electron Devices. 1993 May;40(5):903-9.

[18] Stemme G. Resonant silicon sensors. Journal of Micromechanics and Microengineering. 1991 Jun 1;1(2):113.

[19] Kuntzman ML, LoPresti JL, Du Y, Conklin WF, Naderyan V, Lee SB, Schafer D, Pedersen M, Loeppert PV. Thermal boundary layer limitations on the performance of micromachined microphones. The Journal of the Acoustical Society of America. 2018 Nov 19;144(5):2838-46.

[20] Naderyan V, Raspet R, Hickey C. Analytical, computational, and experimental study of thermoviscous acoustic damping in perforated micro-electro-mechanical systems with flexible diaphragm. The Journal of the Acoustical Society of America. 2021 Oct 14;150(4):2749-56.

[21] Škvor Z. On the acoustical resistance due to viscous losses in the air gap of electrostatic transducers. Acta acustica united with acustica. 1967 Jan 1;19(5):295-9.

[22] Tarnow V. The lower limit of detectable sound pressures. The Journal of the Acoustical Society of America. 1987 Jul;82(1):379-81.
[23] Çaldichoury I, Souli M, Sarradj E, Geyer T, Pin F. Numerical investigation of flow around hairy flaps cylinder using FSI Capabilities. The International Journal of Multiphysics. 2018 Jun 30;12(2):189-208.
[24] Tabiei A, Chowdhury M, Aquelet N, Souli M. Transient response of a projectile in gun launch simulation using Lagrangian and ALE methods. The International Journal of Multiphysics. 2010 Jun 30;4(2):151-73.
[25] Sigrist J. An overview of engineering numerical methods for the dynamic analysis of a nuclear reactor with fluid-structure interaction modelling. The International Journal of Multiphysics. 2009 Mar 31;3(1):31-60.
[26] COMSOL Multiphysics® v. 5.6. COMSOL AB, Stockholm, Sweden. https://www.comsol.com/